Charge and spin transport in two-dimensional materials and their heterostructures

Bettadahalli Nandishaiah, Madhushankar

DOI:
10.33612/diss.135800814

3 Theory of electronic and spin transport in two-dimensional materials

Abstract

In this chapter, the concepts required to understand the electronic and spin transport in two-dimensional materials are introduced. An introduction into the electronic transport properties of bulk and isolated two-dimensional materials is followed by a short introduction to the working principle of a field-effect transistor. Later, the concept of spin injection in non-magnetic materials like graphene is also explained along with a brief explanation on two-channel model for spin transport in a typical spin-valve. Also, the issues of conductivity mismatch and spin relaxation induced by contacts are addressed. Subsequently, the spin transport in graphene, including concepts on spin diffusion equation, non-local spin-valve measurement and Hanle spin precession measurement are described. Later, various spin relaxation mechanisms for spin transport in graphene are introduced. Finally, an overview of the theoretical and experimental studies on spin transport in single and bi-layer graphene, in proximity with TMD, are presented.

3.1 Electronic transport in 2-dimensional materials

In the past four decades, detailed studies have been carried out to understand the electronic charge transport in bulk layered semiconductors[1–3]. The electronic band structure of a bulk layered semiconductor changes depending on the interlayer interaction between its 2D layers and this significantly affects the electronic transport[4,5]. Further, in such a bulk layered semiconductor, one can also expect different charge transport properties (anisotropy) for in-plane (x-y) and out-of-plane (z) directions. Here, the x-y direction corresponds to the charge transport along the length and width of the bulk 2D material, while the z direction is along its thickness[6]. Also, by electrostatically gating such a bulk 2D material via capacitive coupling, one can expect a higher accumulation of charge carriers at the surface which is closer to the gate, in comparison to being depleted in bulk due to charge screening.

Very recently, isolated 2D material of graphene from bulk graphite has been achieved by Novoselov et al.[7]. However, graphene lacks bandgap in its electronic band structure which is quintessential for the realisation of logic-based FETs. This has led to the search for a new class of 2D materials, which are semiconducting, like black phosphorous[5], MoS_2[8], germanane[9] and others. With a plethora of available 2D materials presenting various electrical characteristics, there has been a rise in the study of electronic charge transport in isolated 2D semiconductors[7,10]. This huge interest in isolated 2D semiconductors is mainly due to the reduced screening of charge carriers in comparison to bulk semiconductors, and due to further quantum confinement of charge carriers owing to their two dimensionality[6,10].

3.2 Charge and spin current

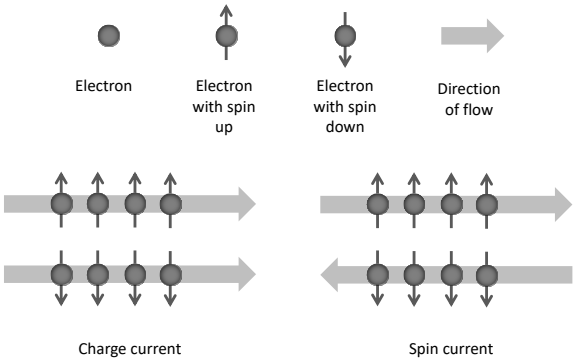

Figure 3.2-1 For a charge current, spin "up" and "down" electrons flow in the same direction while for a spin current, spin "up" and "down" electrons flow in opposite directions.

Electron is an elementary particle of an atom, revolving around the nucleus made up of protons and neutrons. The electrical charge of an electron is negative and is of the order 1.60×10^{-19} C. Electron also has an intrinsic angular momentum, called spin, whose value is $\pm\frac{1}{2}$ depending on: if the spin of the electron is clockwise/up (+) or counter-clockwise/down (-).

Charge current is said to be flowing in a system when electrons, both with spin up and spin down are flowing in the same direction as shown in Figure 3.2-1. The total charge current density ($\vec{J}$) is just the total contribution of up ($\vec{J}_{\uparrow}$) and down ($\vec{J}_{\downarrow}$) spin current density, i.e.

$$\vec{J} = \vec{J}_{\uparrow} + \vec{J}_{\downarrow}. \qquad \text{Equation 3.2-1}$$

Whereas, the spin current results from the flow of spin up and spin down electrons in the opposite direction, as shown in Figure 3.2-1. The total spin current density ($\vec{J}_s$) is just the difference between the up ($\vec{J}_{\uparrow}$) and down ($\vec{J}_{\downarrow}$) spin current density, i.e.

$$\vec{J_s} = \vec{J}_{\uparrow} - \vec{J}_{\downarrow} \qquad \text{Equation 3.2-2}$$

while the current spin polarisation (P_j) is,

$$P_j = \frac{\vec{J}_{\uparrow} - \vec{J}_{\downarrow}}{\vec{J}_{\uparrow} + \vec{J}_{\downarrow}}. \qquad \text{Equation 3.2-3}$$

3.3 Metal oxide semiconductor field-effect transistor

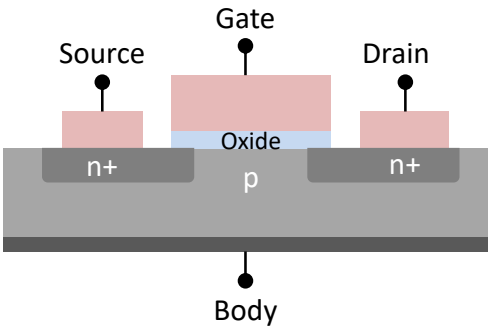

Figure 3.3-1 Cross-sectional view of a MOSFET showing gate, body, source, and drain terminal. Gate is capacitively coupled to the semiconducting channel by a thin dielectric oxide layer.

Metal oxide semiconductor field-effect transistor (MOSFET) is a type of field-effect transistor (FET); it is a three-terminal device consisting of gate, source, and drain electrodes, as shown in the device schematic of Figure 3.3-1. A typical MOSFET consists of a semiconductor connected between a pair of metallic electrodes called source and drain. The conductivity of the semiconductor is capacitively modulated by a metallic gate which is connected to the semiconducting channel through a thin oxide layer, as illustrated in Figure 3.3-1. Conventional silicon transistors are top gated devices along with an additional back gate termed ‘body’ which is usually electrically grounded. MOSFETs are classified depending on the type of charge carriers in the semiconducting channel, i.e. as either n- or p-type corresponding to electron or hole charge transport respectively in the channel.

The transistor illustrated in Figure 3.3-1 is a n-type silicon MOSFET wherein the

semiconductor is hole-doped silicon; highly electron-doped silicon (n+) is used as the source and the drain electrodes. The gate is typically composed of polysilicon with the oxide barrier being silicon-di-oxide. The main application of a MOSFET is its use as a logic switch, realised by turning ON-OFF (represented as 1/0 in digital logic) the current flowing in the semiconducting channel. Some of the factors characterising a good MOSFET are its operational voltage, the rate at which one can turn the current ON-OFF, and the dimension of the transistor. MOSFETs are constantly being developed to achieve better performance by engineering the materials and dimensions of the semiconducting channel, source, drain, and gate.

3.3.1 Graphene FET

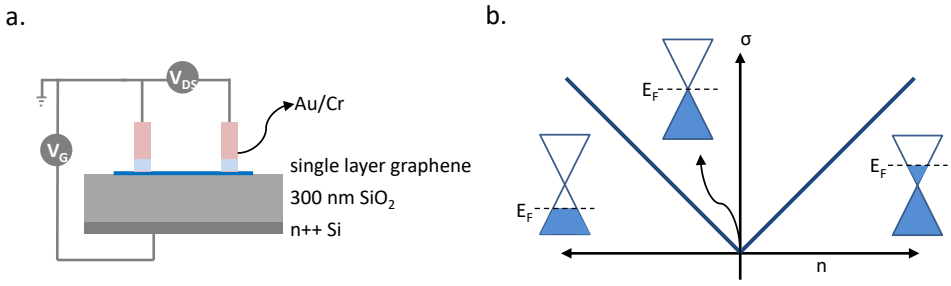

Figure 3.3-2 (a). Device schematic of a FET with graphene channel between source-drain electrodes and a back gate. (b). Sketch of charge carrier conductivity (σ) of graphene FET plotted as a function of charge carrier density (n); inset – band diagram of graphene with fermi energy, E_F.

There has been a constant effort in extending the electric field effect to metals; however, this requires atomically thin metallic films since the electric field at short distances (<1nm) for bulk metals will be screened. Additionally, the charge carrier concentration in a bulk metal is large in comparison to the surface charges that can be induced by the electric field. The first-ever effort to realise the field effect in an atomic layer of semi-metallic graphene was done by Novoselov et al.,[7] wherein, the graphene FET was fabricated and characterised and its device schematic is shown in Figure 3.3-2 (a). Applying a gate voltage (V_G) changes the charge carrier density (n) and the charge carrier type in the graphene, along with shifting the position of the Fermi energy. One can measure the induced charge carrier density by measuring the current (I_{DS}) flowing between the source-drain electrodes by sweeping the voltage (V_{DS}) applied across the source-drain electrodes. The measured conductivity (σ), $\sigma = I_{SD}/V_{SD}$, is plotted as a change in the charge carrier density as shown in Figure 3.3-2 (b). The positive-axis of n corresponds to the electron carrier density (E_F in conduction band) and the negative-axis of n corresponds to the hole carrier density (E_F in valence band). While at zero, it is theoretically expected to have no charge carrier density (E_F in Dirac point) in graphene. The change in conductivity follows the Drude formula[7], $\sigma = ne\mu$ (where, e is the electron charge, and μ is the charge carrier mobility); as a result of this, there is a linear change in σ as a function of change in n, as shown in Figure 3.3-2 (b). Novoselov et al.[7] measured typical values of $\mu \approx 10{,}000$ cm^2/V·s and $n \approx 5 \times 10^{12}$ cm^{-2}, for their graphene FETs.

3.4 Spin injection into non-magnetic materials

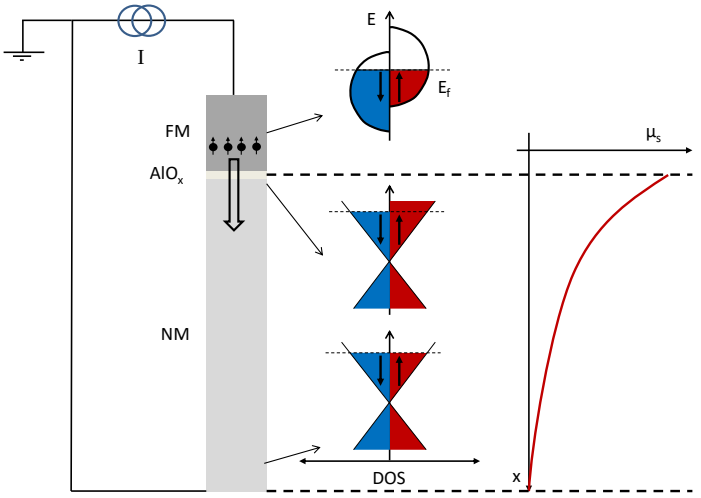

Figure 3.4-1 Spin injection from a ferromagnet (FM) into a non-magnet (NM) is as shown in the left part of the figure. The spin chemical potential in FM, interface (between FM-AlO$_x$ and NM), and the bulk of NM is shown in the centre and an exponential decay of induced spin accumulation from the interface into the bulk of the NM is shown in the right part of the figure.

In this section, the spin injection process from a ferromagnet into a non-magnet is briefly described. Later, the two-channel model for spin transport in a typical spin-valve is explained. Finally, the issue of conductivity mismatch and the spin relaxation induced by contacts are addressed.

One can achieve spin injection into a non-magnet (NM) like graphene by using a ferromagnet (FM) which has a net spin polarisation. In a ferromagnet, there is an imbalance in the density of states for spin-up and spin-down electrons at the Fermi energy, as shown in Figure 3.4-1. This imbalance leads to a difference in conductivity for the spin-up and spin-down channels. For a diffusive system, the conductivity for each spin channel, $\sigma_{\uparrow(\downarrow)}$ can be calculated as,

$$\sigma_{\uparrow(\downarrow)} = g_{\uparrow(\downarrow)}(E_f)e^2 D_{\uparrow(\downarrow)} \qquad \text{Equation 3.4-1}$$

where, $g_{\uparrow(\downarrow)}$ is the density of states at the Fermi energy E_f and $D_{\uparrow(\downarrow)}$ is the diffusivity of each spin channel. The $D_{\uparrow(\downarrow)}$ is defined as, $D_{\uparrow(\downarrow)} = \frac{v_{F\uparrow(\downarrow)} l_{mfp\uparrow(\downarrow)}}{3}$, where $v_{F\uparrow(\downarrow)}$ is Fermi velocity, $l_{mfp\uparrow(\downarrow)}$ is the mean free path length and the factor $\frac{1}{3}$ accounts for the dimensionality of a three-dimensional system.

The net spin imbalance of the FM will be induced into the NM at the interface when current flows from FM into NM, leading to a non-equilibrium state in NM. The induced spin imbalance is termed as spin accumulation (μ_s); the μ_s is measured as the difference in spin

chemical potential for spin-up ($\mu_\uparrow$) and spin-down channels ($\mu_\downarrow$), $\mu_s = \frac{\mu_\uparrow - \mu_\downarrow}{2}$.

Further, there is no spin imbalance in the bulk of the NM, leading to the diffusion of spins from the interface into the bulk of the NM. As the spins diffuse, they also undergo scattering due to their interaction with the impurities or phonons in the bulk of the NM; hence, they undergo relaxation. The spin diffusion length, λ_s is the characteristic distance at which μ_s decays; λ_s and μ_s are related as, $\mu_s \alpha \exp^{-\frac{x}{\lambda_s}}$. The λ_s is related to spin relaxation time τ_s as $\lambda_s = \sqrt{D_s \tau_s}$, where D_s is the spin diffusion co-efficient. In the case of graphene, where electron-electron interaction is the dominant scattering mechanism, $D_s = D_c$, where D_c is the charge diffusion co-efficient. One can write the current spin polarisation (P_j^{NM}) of the NM as $P_j^{NM} = \frac{\mu_s}{j^{NM} R^{NM}}$, where j^{NM} is the charge current density in NM and R^{NM} is the effective resistance of the NM.

One can fabricate the device geometry following Figure 3.4-1 by depositing a thin layer of FM; such as Co, with thickness in the order of ~60 nm and with a length-to-width ratio of 10; on top of graphene. A thin oxide layer of Al_2O_3 as a tunnel barrier between the FM and the graphene prevents the injected spins from flowing back from graphene into the FM.

3.4.1 Two-channel model

A non-magnet (NM) is sandwiched between a pair of ferromagnets (FM) to form a simple two-terminal spin-valve, as shown in Figure 3.4-2. The conductivity for spin-up and spin-down electrons is different in a FM as given by Equation 3.4-1 and therefore the total conductivity of FM is $\sigma = \sigma^\uparrow + \sigma^\downarrow$, where $\sigma^\uparrow$ and $\sigma^\downarrow$ are the conductivities for spin-up and spin-down channel respectively.

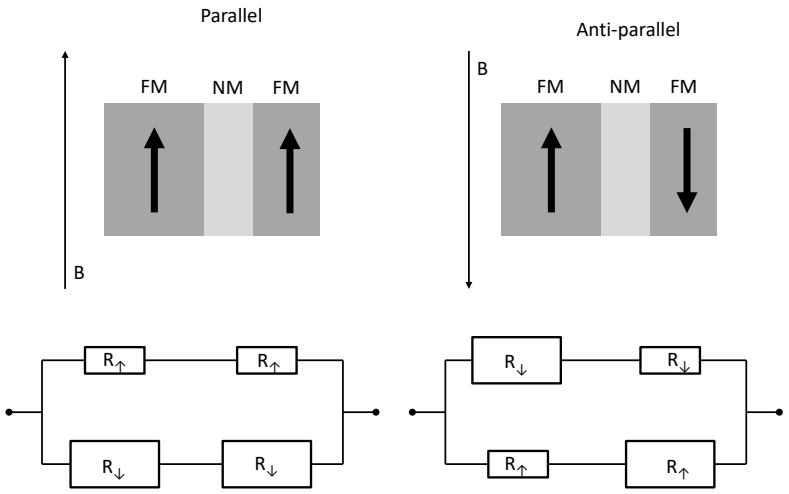

Figure 3.4-2 A two-terminal spin-valve is shown in the top figure with a pair of FM sandwiching a NM. The bottom figure shows the relevant two-channel model for spin-up and spin-down channel for a two-terminal spin-valve.

Resistance for spin-up and spin-down channels of the two-terminal spin-valve is represented as a two-channel model, as shown in the resistance model in Figure 3.4-2. An external magnetic field is applied to magnetise the FM in parallel configuration (the arrows in the figure represent the net magnetisation direction of FM). In this geometry, when the current flows from the left FM to the right FM through the NM (resistance of NM is neglected since it is spin-independent), spin-up channel experiences a low resistance while spin-down channel experiences a high resistance. However, switching magnetisation of one of the FM electrodes from up- to downstate results in an anti-parallel state; as a result, the spin-up and spin-down channels experience a high and low resistance in series as shown in the resistance model of Figure 3.4-2. Thus, the effective resistance for spin-up electrons in parallel configuration is lower than that for anti-parallel state. In principle, there is a flow of spin-polarised current through the spin-valve in parallel configuration, while a net spin accumulation builds up for the anti-parallel configuration which manifests as a voltage drop across the spin-valve.

3.4.2 Conductivity mismatch and contact-induced spin relaxation

So far, the spin injection from a FM into a NM is discussed; however, this spin injection can be significantly affected by the mismatch in spin conductivity for a FM on a NM. Before dwelling on the conductivity mismatch problem, one needs to understand the concept of spin-resistance (R_s).

$$R_s = \frac{\rho\lambda_s}{A} \qquad \text{Equation 3.4-2}$$

spin resistance R_s, is the resistance posed by a material for the flow of spin in it; ρ is the resistivity, λ_s is the spin diffusion length, and A is the cross-sectional area of the material. In the case of the spin injection from a FM into a NM, the spin resistance for FM (R_{FM}) is less than that for NM (R_{NM}); resulting in a backflow of the spins into the FM, which eventually relax in the FM since the lifetime for spins in the FM is short. This backflow of spins from the NM into the FM is due to the conductivity mismatch problem.

One can solve the problem of conductivity mismatch by inserting a high resistive interface barrier between the FM and the NM. The interface barrier is made up of metal oxides such as Al_2O_3, TiO_2, and MgO. The resistance associated with the interface barrier R_b, is higher than that of the NM; and further, R_b is tunable as a function of the barrier thickness.

3.5 Spin transport in graphene

Graphene is an excellent material for the study of spintronics; this is in part due to theoretically predicted large spin relaxation length and time[11,12]. Long spin relaxation length and spin relaxation time in graphene are mainly due to the presence of low spin-orbit coupling and negligible hyperfine interaction. In this section, the study of spin transport in graphene using tools like non-local spin-valve (non-local SV) and Hanle spin precession measurements are briefly discussed.

3.5.1 Spin diffusion equation

The spin diffusion equation describes the spin transport in graphene in the diffusive regime in a steady-state condition as,

$$D_s \nabla^2 \overrightarrow{\mu_s} - \frac{\overrightarrow{\mu_s}}{\tau_s} = \frac{d\overrightarrow{\mu_s}}{dt} = 0 \qquad \text{Equation 3.5-1}$$

where, D_s is the spin diffusion constant, $\overrightarrow{\mu_s} = (\mu_{s,x} + \mu_{s,y} + \mu_{s,z})$ is the spin accumulation in three-dimension, and τ_s is the spin relaxation time. The first term represents the spin diffusion process, and the second term represents the process of spin relaxation. Equation 3.5-1 can be solved for one-dimensional (1D) spin transport, for example along the x-direction resulting in $\mu_s = \mu_s^o(Ae^{-\frac{x}{\lambda_s}} + Be^{+\frac{x}{\lambda_s}})$, where the A and B are the constants defined by the boundary condition and μ_s^o is the injected spin accumulation. For an 1D channel x which is infinitely long, i.e. $x = \pm\infty$ is taken as the boundary condition, the obtained general solution is $\mu_s = \mu_s^o e^{\frac{-|x|}{\lambda_s}}$, where λ_s is the spin diffusion length. According to this general solution, the injected spin accumulation in graphene decays exponentially along the length of the graphene channel, becoming 0 at $x = \pm\infty$. The spin accumulation can be estimated by fabricating multiple FM detector electrodes, spaced at different points from a common spin injecting electrode, and measuring the spin accumulation at each point. However, this method is not very effective since the detector electrodes placed in between a pair of injector-detector electrodes can affect the spin transport significantly (i.e. if the contacts are invasive as explained in detail in section 3.4.2). Further, the detector electrodes can also have different spin polarisation affecting the spin detection.

If one considers the spin relaxation in an applied magnetic field $\vec{B}$ (perpendicular to the plane of graphene), the spins precess around the $\vec{B}$ and this dynamics can be included in Equation 3.5-1 as,

$$D_s \nabla^2 \overrightarrow{\mu_s} - \frac{\overrightarrow{\mu_s}}{\tau_s} + \overrightarrow{\omega_L} \, X \, \overrightarrow{\mu_s} = \frac{d\overrightarrow{\mu_s}}{dt} = 0 \qquad \text{Equation 3.5-2}$$

where, the spins precess with a Larmor frequency $\overrightarrow{\omega_L} = \frac{g\mu_B}{\hbar\vec{B}}$; μ_B is the Bohr magneton and g is the gyromagnetic factor (g-factor, g=2 for free electrons). Equation 3.5-2 is the Bloch equation for spin transport in three-dimensional systems.

3.5.2 Non-local spin-valve measurement

In a local spin-valve measurement discussed in detail in section 3.4.1, the current is flowing through the FM/NM/FM leading to a voltage drop across the multilayer. In this case, the voltage drop measured includes both the effects of spin and charge current flowing through the multilayer. With the presence of both the effects, the charge current flow can be dominating the spin current flow, and in such a case, the charge current flow masks the spin-related effects[13]. To avoid this problem, one needs to achieve pure spin current flowing in the NM. The pure spin current is the flow of spin-up electrons in one direction and spin-down

electrons in the opposite direction, while the net charge current flow being zero.

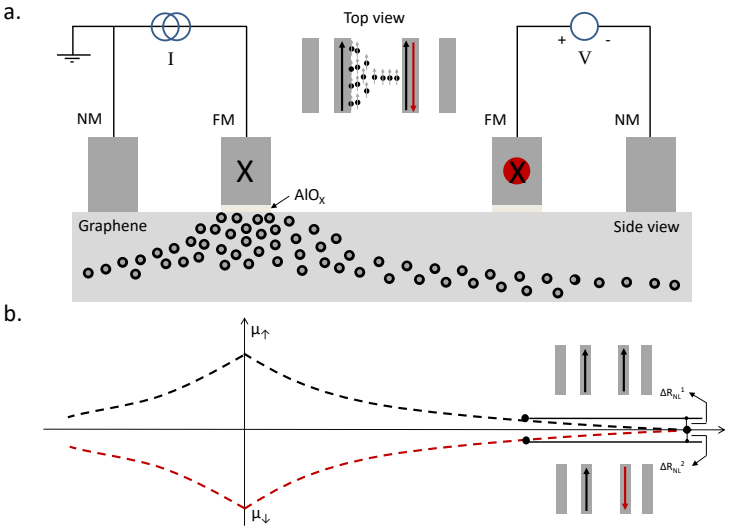

Figure 3.5-1 (a). Schematic of a non-local SV geometry with a pair of FM and the NM on a graphene flake. The applied magnetic field is along the plane of graphene, i.e., along the length of the FM (indicated as X). Here, the current injector and the voltage detector circuits are separate. Further, spin accumulation created at the injector FM decays along the length of the graphene channel in either direction. (b). Shows the distribution of spin chemical potential along the length of the graphene channel for parallel and anti-parallel configurations of injector-detector FM magnetisation.

In a non-local SV measurement, the current injector circuit and the voltage detector circuit are separate, i.e., the voltage drop of the diffusing spins in the NM is determined non-locally. The construction of a lateral non-local SV geometry is shown in Figure 3.5-1 (a), with a pair of FM and NM placed on a graphene channel. An external magnetic field is applied to the contacts to align the magnetisation of the FMs parallel to each other. An electrical current of magnitude 'I' flows in the injector circuit through the FM/graphene/NM. Since the external magnetic field has magnetised the FM electrodes in the injector circuit, the electrical current flowing through the FMs is spin-polarised and creates a build-up of spin chemical potential (μ_s^0) in the graphene at the FM interface,

$$\mu_s^0 = \frac{eP_i I \rho \lambda_s}{2W}$$ Equation 3.5-3

where e is the electron charge, P_i is the polarisation of the injector, I is the electrical charge current flowing, ρ is the resistivity, W is the width of the channel, and λ_s is the spin diffusion length.

The non-local voltage (V_{NL}) detected is, $V_{NL} = \frac{P_d \mu_s(L)}{e} - \frac{P'_d \mu'_s(L')}{e}$, which is the electrochemical potential difference between the FM detector electrode and the NM reference electrode which is placed at a distance L and L′ respectively from the FM injector electrode.

P_d and P_d' is the polarisation of the FM and NM detector electrodes respectively. In our case, as the outer reference contact is a NM, and it has a P_d'=0; which implies that the measured $V_{NL} = \frac{P_d \mu_s(L)}{e}$. By applying a reverse magnetic field, one can flip the magnetisation of the detector electrode in to the anti-parallel state, thereby leading to a change in the measured non-local voltage (V_{NL}). Further, the injected spins decay exponentially along the length of the channel as explained in section 3.5.1, and the non-local resistance measured at the detector circuit is $R_{NL} = \frac{V_{NL}}{I}$. Considering both the, we can write R_{NL} as:

$$R_{NL} = \pm \frac{P_i P_d \rho \lambda_s}{2W} e^{-\frac{L}{\lambda_s}}$$ Equation 3.5-4

wherein '+' is the R_{NL} measured for parallel orientation of FMs, i.e. ↑↑, and '-' is the R_{NL} measured for anti-parallel orientation of FMs, i.e. ↑↓, as shown in Figure 3.5-2. The measured R_{NL} as a function of applied magnetic field is as shown in Figure 3.5-2. If the NMs (used as the outer electrode) are replaced by FMs, then multiple switches corresponding to the switching of these extra FMs will be reflected in the measured R_{NL} as a function of applied magnetic field. The measured R_{NL} can also include a non-zero background signal, caused by an inhomogeneous current flow through the oxide barriers[14].

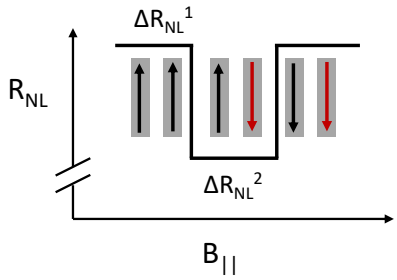

Figure 3.5-2 The switching of FM electrodes represented as a change in non-local resistance as a function of an applied magnetic field.

To summarise, the injection and detection of in-plane spins were described in this section. However, it deems necessary to investigate the injection and detection of out-of-plane spins also. In light of this, a new technique of oblique spin-valve measurement to inject and detect both the in-plane and out-of-plane spins, and determine their spin lifetimes is presented in subsection 3.5.2.1.

3.5.2.1 Oblique spin-valve measurement

In order to accurately determine the spin lifetime for in-plane ($\tau_{||}$) and out-of-plane spins ($\tau_{\perp}$) even in the possible presence of a background charge-signal, we have developed a new tool in-house called the Oblique Spin-Valve (OSV) measurement. For the OSV measurement, we follow a similar measurement procedure as in the SV measurement. However, for the magnetisation reversal in FM electrodes, a magnetic field B is applied making an angle θ_B in the y-z plane with respect to the easy-axes of the FM electrode (along y-axis), as shown in

Figure 3.5-3 (a); this is in contrast to applying B in the plane of graphene and parallel to FM as in SV measurement shown in Figure 3.5-1. As a result, the magnetisations of the FM electrodes also make a finite angle θ with their easy axis; and this way, both in-plane and out-of-plane spins are injected and detected in the spin-transport channel. The in-plane magnetic field ~Bcos θ_B is responsible for the magnetisation switching of C2 and C3 which are the injector and detector FMs. In the event of magnetisation reversal at a magnetic field in the OSV measurements, the spin-signal change would appear as a sharp switch in R_{NL}. However, the magnetic field dependent background signal does not change.

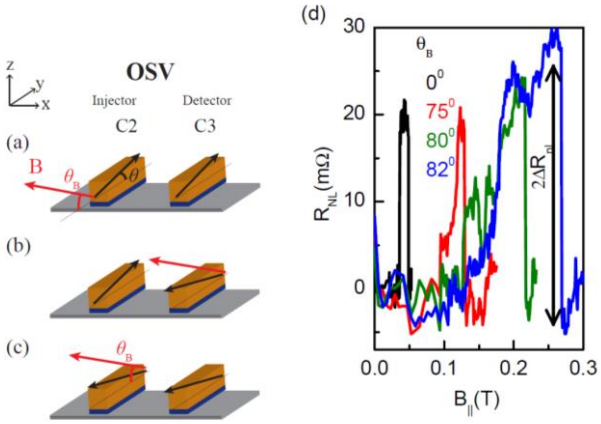

Figure 3.5-3 (a-c). Steps for Oblique Spin-valve (OSV) measurements. The magnetisation vector for the injector and detector (in black) makes an angle θ with the easy axis; the applied magnetic field B (red vector) for the magnetisation reversal remains fixed at an angle θ_B throughout the measurement. The magnetisation reversal for the detector and the injector are shown in (b) and (c), respectively. (d). OSV measurements at different θ_B values for the injector-detector separation L = 1 μm. The OSV spin-signal ΔR_{NL} is half of the magnitude of the switch, labelled with the black arrow. The increase in the spin-valve signal magnitude at higher θ_B confirms the presence of a large spin-relaxation anisotropy. A background signal (0.5-1 Ω) has been removed from the measured signal for a clearer representation.

In an OSV measurement, we measure a fraction of non-local resistance arising from both in-plane ($R_{NL}^{\parallel}$) and out-of-plane ($R_{NL}^{\perp}$) spin diffusion. The OSV spin-signal, ΔR_{NL}, consists of two components: an in-plane spin-signal component proportional to $R_{NL}^{\parallel}(\cos\theta)^2$, and an out-of-plane spin-signal component proportional to $R_{NL}^{\perp}(\sin\theta)^2$; both of which get dephased by the applied magnetic field Bsin θ_B and Bcos θ_B respectively,

$$\Delta R_{NL} = R_{NL}^{\parallel}(\cos\theta)^2\zeta_{\parallel}(B\sin\theta_B) + R_{NL}^{\perp}(\sin\theta)^2\zeta_{\perp}(B\cos\theta_B) \qquad \text{Equation 3.5-5}$$

where $\zeta_{\parallel(\perp)}$ is the functional form for the in-plane (out-of-plane) spin precession dynamics. There is an enhancement in the dephasing of the in-plane spin-signal $R_{NL}^{\parallel}$ at larger θ_B. Conversely, there is a suppression in the dephasing of the out-of-plane spin-signal $R_{NL}^{\perp}$ at larger θ_B. Also, θ increases with θ_B. Therefore, $R_{NL}^{\perp}$ dominates the ΔR_{NL} at higher θ_B and acquires a similar form as in Equation 3.5-4.

The switches in OSV measurement performed for BLG on WS_2 are as shown in Figure 3.5-3

(d). In order to verify our hypothesis, we first measure the in-plane spin-valve signal $\Delta R_{NL} = R_{NL}^{\parallel}$ at $\theta_B = 0^\circ$ for L = 1 μm, and then measure R_{NL} at different θ_B values. Figure 3.5-3 (d) shows the measurement summary. Here, we observe an increase in ΔR_{NL} up to 1.5 times with respect to ΔR_{NL} at $\theta_B = 0^\circ$ by increasing θ_B. This result is remarkable in the way that it is possible to observe a clear enhancement even with a small fraction of $R_{NL}^{\perp}$, i.e. $\alpha\ R_{NL}^{\perp}$ $(\sin\theta)^2$ contributing to ΔR_{NL}.

Note: Following Equation 3.5-5 for $R_{NL}^{\perp} \leq R_{NL}^{\parallel}$, we would never observe an increase in R_{NL}.

3.5.3 Hanle spin precession measurement

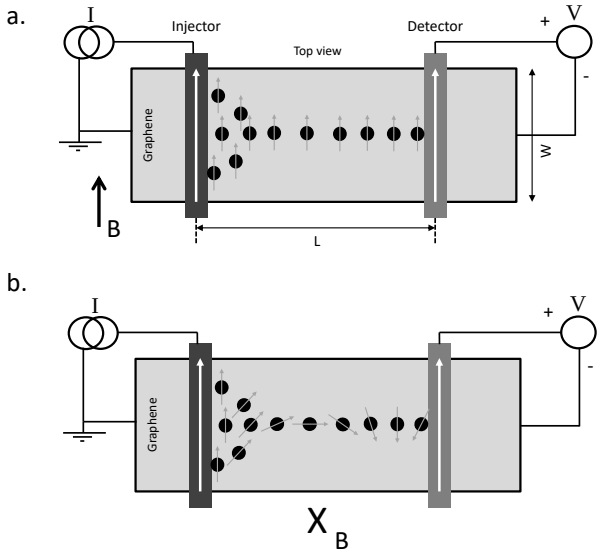

Figure 3.5-4 (a). Schematic of non-local spin transport from the injector to the detector with an in-plane magnetic field (B) applied to magnetise the injector-detector FM electrodes. (b). Schematic of non-local spin transport from the injector to the detector with an out-of-plane magnetic field (B) which precesses the spins travelling across graphene.

Hanle spin precession measurement is performed to determine the spin transport parameters like spin diffusion length (λ_s) and spin diffusion time (τ_s). To carry out the Hanle spin precession measurement, the ferromagnetic electrodes (injector and detector) are first magnetised in a specific configuration, i.e. in parallel or anti-parallel state, by applying an in-plane magnetic field, as shown in Figure 3.5-4 (a). The spins travelling across the graphene channel from the injector towards the detector (which are separated by a distance L) have a probability distribution as a function of time, ($P_D(t)$) given by:

$$P_D(t) = \frac{1}{\sqrt{4\pi D_s t}} e^{-\frac{L^2}{4D_s t}} \qquad \text{Equation 3.5-6}$$

where D_s is the spin diffusion coefficient.

During the spin transport in graphene, spins undergo relaxation and the probability of spins relaxing (P_τ) during their flight is included by multiplying the Equation 3.5-6 by the term $P_\tau = e^{-t/\tau_s}$. Further, a magnetic field (B) perpendicular to the plane of graphene is applied, as shown in Figure 3.5-4 (b). This magnetic field causes the spins to precess around the applied field, accounted by the term cos(ωt) where ω is the frequency at which the spins precess. The frequency of spin precession is related to the applied magnetic field by $\omega = \frac{g\mu_B}{\hbar} B_o$, where g is the Landé g-factor, μ_B is the Bohr magneton, and ħ is the reduced Planck's constant. The probability distribution of spins at the detector electrode including spin diffusion, relaxation, and precession are as follows:

$$P(t) = \frac{1}{\sqrt{4\pi D_s t}} e^{-\frac{L^2}{4D_s t}} e^{-\frac{t}{\tau_s}} \cos(\omega t). \qquad \text{Equation 3.5-7}$$

The projection of the average spin accumulation (μ_s) at the detector over all possible diffusion times is obtained by:

$$\mu_s(L, B) = 2\sqrt{\frac{D_s}{\tau_s}} \mu_s^0 \int_0^\infty P(t) dt. \qquad \text{Equation 3.5-8}$$

The above integral can be numerically solved. Using Equation 3.5-4, an analytical expression of measured non-local resistance (R_{NL}) is obtained as:

$$R_{NL}(L, B) = \pm \frac{P_i P_d R_{sq} D_s}{W} \mathrm{Re}\left\{ \frac{1}{2\sqrt{D_s}} \frac{e^{-L\sqrt{\lambda_s^{-2} - i\frac{\omega}{D_s}}}}{\sqrt{\tau_s^{-1} - i\omega}} \right\}. \qquad \text{Equation 3.5-9}$$

In an actual experiment, the R_{NL} measured at the detector, as a function of an applied perpendicular magnetic field, is fit in the above equation to obtain spin-related information like spin relaxation length (λ_s) and spin diffusion coefficient (D_s).

The spin lifetime (τ_s) estimated from this method is for the spins which are in the plane of graphene, i.e. in-plane spin lifetime ($\tau_\parallel$). However, spins which are out of the plane of graphene can also be studied in order to compare their spin lifetimes ($\tau_\perp$) to that of in-plane spins. For an isotropic system, $\tau_\parallel = \tau_\perp$. However for an anisotropic system, $\tau_\parallel \neq \tau_\perp$; hence, it is essential to estimate both $\tau_\parallel$ and $\tau_\perp$ to calculate the spin lifetime ratio, $\zeta = \frac{\tau_\perp}{\tau_\parallel}$. $\tau_\perp$ can be estimated using different Hanle spin precession techniques like (explained in detail in the following sub-sections):

1. Hanle spin precession measurement at high magnetic field
2. Oblique Hanle spin precession measurement
3. In-plane Hanle spin precession measurement

Note: Oblique spin-valve measurement described in section 3.5.2.1 is another technique that

can be used to determine the $\tau_\perp$.

3.5.3.1 Hanle spin precession measurement at high magnetic field

In section 3.5.3, the injection, transport, and precession of spins in the plane of graphene were discussed. Following it up, this section includes a discussion on the spins which are out-of-plane of the graphene. Out-of-plane spins can be injected electrically by controlling the magnetisation direction of the FM electrodes via an external magnetic field. Studying of spin transport properties of both in-plane and out-of-plane spins is essential in understanding the anisotropy in their spin relaxation time. By applying a magnetic field ($B_\perp$) in the out-of-plane direction aligns the magnetisation of the FM in out-of-plane direction at high $B_\perp$ and thus injecting out-of-plane spins into the graphene. For the FM electrodes with a thickness of 65 nm, their magnetisation can be aligned fully in the out-of-plane direction at $B_\perp \approx 1.5$ T. At $B_\perp \geq 0.3$ T, the magnetisation of the FM makes an angle $\theta > 10^{\circ}$ with the easy-axis of the FM electrode (which is in-plane); further, the θ increases with the increasing $B_\perp$.

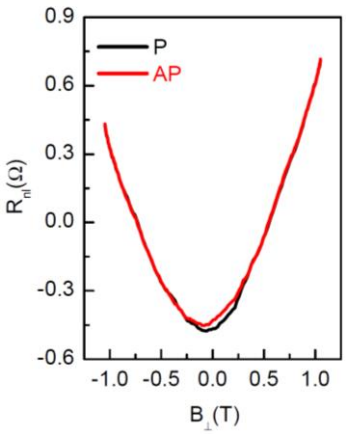

Figure 3.5-5 Parallel (P) and anti-parallel (AP) Hanle curves for L = 1 μm (back gate voltage is 0 V) show a strong increase in the nonlocal resistance (R_{NL}) with the applied out-of-plane magnetic field $B_\perp$, indicating a large spin-relaxation anisotropy and a high spin-relaxation time for the out-of-plane spins. Signs of parallel (P) and anti-parallel (AP) configurations are reversed because one electrode has a negative contact-polarisation for in-plane spins.

Figure 3.5-5 shows an increase in the R_{NL} with the applied out-of-plane magnetic field $B_\perp$. This is due to the injection and transport of the non-precessing out-of-plane spin-signal component which would increase with increasing $B_\perp$, owing to the FMs magnetisation aligning towards the out-of-plane direction. From this measurement, we can estimate the spin lifetime for out-of-plane spins ($\tau_\perp$) by removing the contribution from the in-plane spin-signal and the background charge (magneto) resistance by fitting the R_{NL} with the following equation,

$$R_{NL}(B_\perp) = \frac{P_i P_d \rho \lambda_S^\perp \sin\theta^2}{2W} e^{-\frac{L}{\lambda_S^\perp}} \qquad \text{Equation 3.5-10}$$

where $\lambda_s^{\perp}$ is the spin relaxation length for out-of-plane spins, and θ is the angle of the FM magnetisation to the easy-axis of the FM electrode.

One should note that there is a large contribution of magneto-resistance (MR) at a high out-of-plane magnetic field. To better estimate the $\tau_{\perp}$, one needs to remove the effect of MR from the measured R_{NL}. Hanle spin precession measurements can also be performed by applying an in-plane magnetic field[15] which precess the spins in both in-plane and out-of-plane direction to determine both $\tau_{\parallel}$ and $\tau_{\perp}$ simultaneously (in this case, there is a negligible contribution of MR at a high in-plane magnetic field).

3.5.3.2 Oblique Hanle spin precession measurement

Here, we will discuss the method described in the report by Raes et al.[15] presenting a way to extract spin lifetime for electron spins travelling out-of-plane of the graphene, i.e., $\tau_{\perp}$ by using oblique Hanle spin precession measurement.

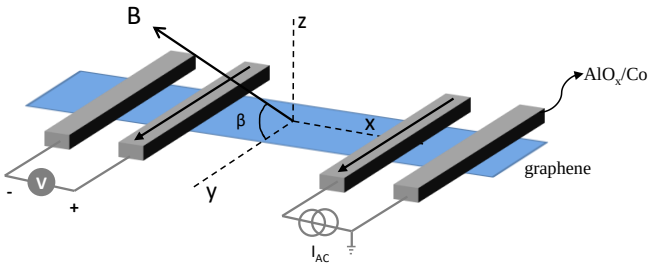

Figure 3.5-6 Device schematic of graphene contacted with FM contacts. Here a magnetic field B is applied at an angle β to the y-z plane of graphene.

The FM electrodes are magnetised (injector and detector) along the y-axis in a specific configuration, i.e., parallel or anti-parallel state, by applying an in-plane magnetic field as explained in section 3.5.3 and shown in Figure 3.5-4 (a). However, for oblique Hanle spin precession measurement, unlike in section 3.5.3 where we applied a magnetic field which is perpendicular to the plane of graphene, we apply a magnetic field at an angle β to the y-z plane of graphene as shown in Figure 3.5-6. In this scenario, the spins injected at the FM injector electrode (in-plane) diffusing towards the FM detector electrode start to precess with both in-plane and out-of-plane spin component. Hence, the spin precession dynamics for B applied with $0<\beta<90^{\circ}$ is sensitive to both $\tau_{\parallel}$ and $\tau_{\perp}$. With increasing B, the spin component which is perpendicular to the applied magnetic field de-phases. For $B>B_d$, where B_d is the de-phasing field, the spin component which is parallel to the applied field B alone remains this is picked up as the non-local signal at the FM detector electrode. The spin lifetime of the resulting component which is parallel to the applied field is represented as $\tau_{s\beta}$ and follows the relationship,

$$\frac{\tau_{s\beta}}{\tau_{\parallel}} = \left((\cos\beta)^2 + \frac{1}{\zeta}(\sin\beta)^2\right)^{-1} \qquad \text{Equation 3.5-11}$$

where, $\zeta = \frac{\tau_\perp}{\tau_\parallel}$ is the spin lifetime anisotropic ratio. $\tau_\parallel$ is measured using conventional Hanle spin precession measurement as explained in section 3.5.3; alongside knowing $\tau_\parallel$ and studying the dephased non-local signal as a function of β, one can extract ζ using Equation 3.5-11.

A detailed explanation of this technique can be found in the report by Raes et al.[15]

3.5.3.3 In-plane Hanle spin precession measurement

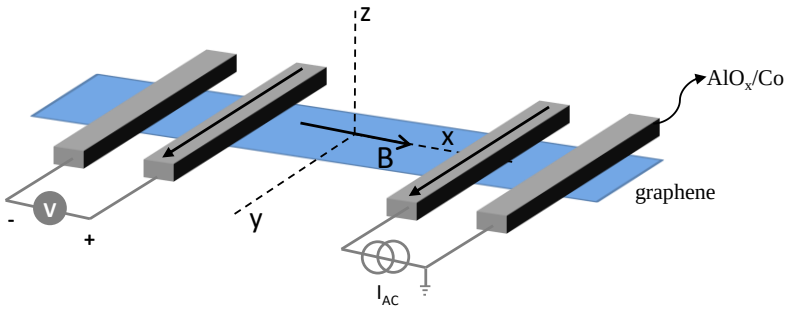

Figure 3.5-7 Device schematic of graphene with FM contacts. Here, a magnetic field B is applied along the x-axis which is perpendicular to the magnetisation axis of FM and is in the plane of graphene.

The out-of-plane spin lifetime ($\tau_\perp$) can also be estimated by the in-plane Hanle spin precession measurement. Unlike as discussed in section 3.5.3 and 3.5.3.2: where the magnetic field B is applied perpendicular or at an angle to the plane of graphene respectively; for in-plane Hanle spin precession measurement, B is applied along the x-axis as shown in Figure 3.5-7 wherein B is perpendicular to the magnetisation axis of the FM and is in the plane of graphene. In this scenario, the spins injected along the y-axis precess in the y-z plane. Therefore, the in-plane Hanle precession measurement is sensitive not only to $\tau_\parallel$ but also to $\tau_\perp$.

The time-independent Bloch-diffusion equation is used to model and analyse the in-plane Hanle spin precession measurement:

$$D_s \frac{d^2\vec{\mu}_s}{dx} - \hat{\tau}^{-1}\vec{\mu}_s + \frac{g\mu_B}{\hbar}\vec{\mu}_s \times \vec{B} = 0 \qquad \text{Equation 3.5-12}$$

where, D_s is the spin diffusion coefficient, $\vec{\mu}_s = (\mu_{s,x}, \mu_{s,y}, \mu_{s,z})$ is the spin accumulation for spins oriented in the three Cartesian coordinates $\hat{x}$, $\hat{y}$, and $\hat{z}$, g is the gyromagnetic factor ($g = 2$), μ_B is the Bohr magneton, and $\vec{B}$ is the external applied magnetic field. The matrix $\hat{\tau}^{-1}$ is defined as,

$$\hat{\tau}^{-1} \equiv \begin{pmatrix} \frac{1}{\tau_{\parallel}} & 0 & 0 \\ 0 & \frac{1}{\tau_{\parallel}} & 0 \\ 0 & 0 & \frac{1}{\tau_{\perp}} \end{pmatrix} \qquad \text{Equation 3.5-13}$$

where $\tau_{\parallel}$ and $\tau_{\perp}$ are the spin lifetimes for spins oriented along the in-plane and out-of-plane directions, respectively. $\tau_{\parallel}$ is estimated by using the perpendicular Hanle spin precession measurement, as explained in section 3.5.3. Equation 3.5-13 is substituted in Equation 3.5-12 and solved for $\tau_{\perp}$ using a numerical finite element method using a commercial software package like COMSOL. After estimating both the values $\tau_{\parallel}$ and $\tau_{\perp}$, one can estimate the spin relaxation time ration as $\zeta = \frac{\tau_{\perp}}{\tau_{\parallel}}$.

A detailed explanation of this technique and its comparison with both the perpendicular and oblique Hanle spin precession measurement can be found in the report by Ringer et al.[16].

3.6 Spin relaxation in graphene

The decay of spin-polarised electrons in metals and semiconductors is mainly due to either the spin-flip scattering or spin dephasing. The relaxation mechanisms thus involved are the discussed in the following subsections.

3.6.1 Elliot-Yafet (EY) mechanism

Elliot-Yafet (EY) mechanism is observed in semiconductors and metals with inversion symmetry. Here, the spins scatter because of impurities or phonons; the momentum scattering causing a spin-flip. In this case[17], the spin relaxation time (τ_s) is directly proportional to the momentum scattering time (τ_p), i.e. $\tau_s \propto \tau_p$.

3.6.2 D'yakonov-perel mechanism

D'yakonov-perel mechanism is observed in semiconductors without any centre of inversion symmetry, thus presenting an effective magnetic field. The spin associated with the electron moving in a semiconductor precesses around this magnetic field; and eventually when it undergoes scattering, the spins precession angle changes. In such a case[17], the spin relaxation time (τ_s) is inversely proportional to the momentum scattering time (τ_p), i.e. $\tau_s \propto \tau_p^{-1}$.

3.6.3 Hyperfine interaction

Hyperfine interaction is present in the materials made up of atoms with a nuclear spin. When the electron spin interacts with an ensemble of nuclear spins, it leads to an eventual spin-flip and spin dephasing. Naturally available graphene is composed of both ^{12}C (99%) and ^{13}C (1%) isotopes, however only ^{13}C has nuclear spins. Due to the low percentage of ^{13}C in the graphene, the hyperfine interaction can be considered negligible.

3.6.4 Rashba spin-orbit coupling

Rashba type spin-orbit coupling (SOC) is a type of SOC which arises in the presence of an internal or external electric field. Rashba type SOC is only present in materials with broken inversion symmetry, wherein, the presence of an electric field breaks the inversion symmetry. In the presence of Rashba type SOC, an electric field is perceived as an effective magnetic field by a moving electron, leading to the spin precession of the electron around this magnetic field. This effective magnetic field is the Rashba field B_R which is defined as[18],

$$B_R = 2\alpha_R(\varepsilon)\frac{k_F}{g\mu_B} \qquad \text{Equation 3.6-1}$$

where α_R is the Rashba parameter which can be tuned by the electric field ε, k_F is the wavenumber at the Fermi level, $g \approx 2$ is the g-factor and μ_B is the Bohr magneton.

3.7 Spin-orbit interaction in single and bilayer graphene in the proximity of TMD

In this section, a brief overview of the theoretical and experimental studies on the single and bi-layer graphene, in proximity to TMD, are presented.

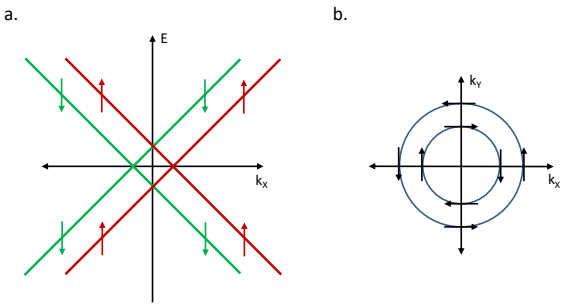

Figure 3.7-1 (a). Band splitting in mono-layer graphene due to the presence of Rashba type SOC. (red and green correspond to sub-bands for up and down spins). (b). Top view of the in-plane spin components in the k_X-k_Y plane.

3.7.1 Spin-orbit interaction in single-layer graphene

The electronics band structure of the graphene in the vicinity of K(K′) is described by the Hamiltonian $H_o=\hbar v_F(k\sigma_x k_x+\sigma_y k_y)$ (without considering any spin-orbit interaction). Here, v_F is the Fermi velocity, k_x and k_y are the Cartesian components of the electron wave vector measured from K(K′), and σ_x and σ_y are the Pauli matrices acting on the so-called pseudospin space formed by the two triangular sublattices of the graphene. This results in an energy band diagram described by a two-dimensional Dirac equation which is linear in dispersion and centred on the hexagonal corners of the honeycomb lattice of a Brillouin zone.

In 2006, Min et al.[19] considered the microscopic tight-binding model; and by using second-

order perturbation theory they derived explicit expressions considering the intrinsic and Rashba spin-orbit interaction in an isolated graphene sheet as,

$$\lambda_{SO} = \frac{|s|}{18(sp\sigma)^2}\xi^2 \quad \text{Equation 3.7-1}$$

$$\lambda_R = \frac{eEz_0}{3(sp\sigma)}\xi \quad \text{Equation 3.7-2}$$

where |s| and (spσ) are tight-binding model parameters, z_o is proportional to the atomic size of the carbon, ξ is the atomic spin-orbit interaction strength, λ_{SO} and λ_R are the coupling constants for intrinsic and Rasbha spin-orbit coupling, and E is a perpendicular external electric field which lifts inversion symmetry in the graphene plane (E could also be produced by the doping of graphene by substrate or capping layer, or also by the atomic length scale charge re-arrangement at the graphene/substrate or the graphene/capping layer interfaces). It was found that[19], the intrinsic and the Rashba spin-orbit interactions arise from mixing of σ and π bands: due to the atomic spin-orbit interactions alone in the case of λ_{SO} as shown in Equation 3.7-1, and due to the combination of atomic spin-orbit and Stark interaction in the case of λ_R as shown in Equation 3.7-2. The intrinsic SOC in graphene leads to a bandgap opening of 1 μeV suggesting that the quantum spin Hall effect will be observable in ideal samples only at temperatures below ~0.01 K in a zero-field limit.

In 2009, Gmitra et al.[20] revealed that the intrinsic SOC in graphene was caused by the d and higher orbitals, (in the first order of the respective atomic splitting on inclusion of SOC) whose contribution is dominant due to symmetry reasons, instead of the mixing of σ and π bands as assumed by Min et al.[19]. The intrinsic SOC is defined by the effective Hamiltonian $H_o=\lambda_I k\sigma_z s_z$, where s_z is the spin Pauli matrix and λ_I is the intrinsic SOC strength. Gmitra et al.[20] calculated the intrinsic SOC to be around 24 μeV. The extrinsic SOC of the Rashba type in graphene can be described by the Hamiltonian $H_R=\lambda_R(k\sigma_x s_y-\sigma_y s_x)$, where λ_R is the Rashba SOC strength. The SOC in graphene does not depend on the magnitude of the electron momentum, as the electrons at K and K' have a constant velocity. The electronic bands near K(K') are split as a result of the induced Rashba type SOC; band splitting in the conduction band at K point is as shown in Figure 3.7-1 (a), and the top view of the in-plane spin components in the k_X-k_Y plane is shown in Figure 3.7-1 (b). Rashba induced SOC was proven to be dominated solely by the σ-π mixing. The electric field-induced Rashba SOC was found to be 10 μeV per V/nm.

3.7.2 Spin-orbit coupling in single-layer graphene in the proximity of TMD

Transition metal di-chalcogenides (TMD), like tungsten di-selenide (WSe_2), are two-dimensional in nature and possess strong intrinsic SOC. They can be mechanically cleaved and stacked with graphene to form clean 2D van-der-Waal heterostructure. Such a heterostructure provides the possibility to realise TMD proximity induced SOC in graphene, in the orders of few meV[21,22], without compromising on the phenomenal charge transport properties of graphene.

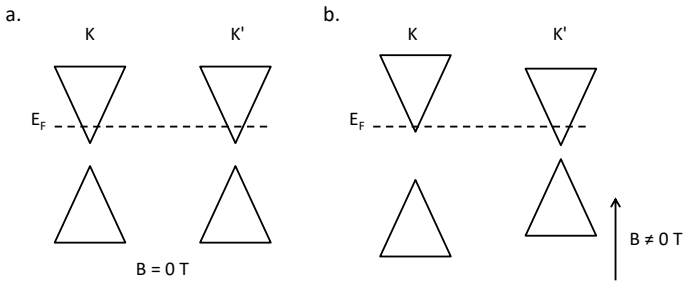

Figure 3.7-2 Schematics of the valley-Zeeman effect for graphene on TMD with a magnetic field (B) applied perpendicular to the plane of graphene; when (a) B=0, and (b) B≠0. The orbital magnetic moments, having opposite signs for K and K' valleys, interact with B, inducing a different number of spin up and down electrons at the Fermi energy in the K and K' valleys as shown in (b).

At the interface of TMD and graphene, the inversion symmetry in graphene is broken; this along with a TMD proximity induced SOC opens a bandgap in graphene with spin split and valley locked states. This is because, d-orbitals of the TMD can couple with π band of the graphene inducing a large SOC in graphene as well as a Rashba SOC at the TMD-graphene interface, both of the order ~10 meV[21,23]. The orbital magnetic moments (lying perpendicular to the graphene plane), having opposite signs for K and K' valleys, interact with the magnetic field applied perpendicular to the plane of graphene; the interaction induces a different number of spin up and down electrons at the Fermi energy in the valleys, which is termed as valley-Zeeman effect, as shown in Figure 3.7-2 (b). Further, with the application of a perpendicular electric field, the spin transport in graphene in contact with TMD experiences an in-plane Rashba field. Hence, the effective Hamiltonian for a graphene-TMD heterostructure is represented by,

$$H = H_0 + H_I + H_\lambda + H_R \qquad \text{Equation 3.7-3}$$

where H_0 is the Hamiltonian for a pristine graphene without SOC, H_I is the Hamiltonian for the intrinsic SOC in graphene, and H_λ and H_R are the SOC Hamiltonians for valley-Zeeman and Rashba type SOC respectively.

The interplay between the Rashba (λ_R) and the valley-Zeeman type SOC (λ_V) can be detected by the anisotropy in the spin relaxation time for in-plane ($\tau_\parallel$) and out-of-plane ($\tau_\perp$) spin transport in graphene in contact with the TMD. The in-plane spins experience a motion-narrowing, while scattering from one valley to another, since their sense of precession is reversed due to the reversal of the SOC field direction in each valley. Further, the in-plane spin relaxation also includes contributions from the overall momentum scattering. This is manifested by,

$$\frac{1}{\tau_\parallel} = \frac{4\lambda_V^2}{\hbar^2}\tau_{iv} + \frac{2\lambda_R^2}{\hbar^2}\tau_p \qquad \text{Equation 3.7-4}$$

where τ_{iv} is the inter-valley scattering time, τ_p is the momentum scattering time, λ_V is the valley-Zeeman SOC strength, λ_R is the Rashba SOC strength, $\tau_\parallel$ is the in-plane spin relaxation

time, and ħ is the reduced Planck constant. The out-of-plane spins are de-phased by the in-plane Rashba field with motion narrowing during momentum scattering which is manifested by,

$$\frac{1}{\tau_\perp} = \frac{4\lambda_R^2}{\hbar^2}\tau_p. \qquad \text{Equation 3.7-5}$$

As the spin transport in graphene in contact with the TMD experiences both inter-valley (iv) and momentum (p) scattering, it has been theoretically[24] predicted that their lifetime ratio is $\tau_{iv} \approx 5\tau_p$. Considering both the effects of the Rashba spin-orbit coupling and inter-valley/momentum scattering, the spin lifetime anisotropy is,

$$\frac{\tau_\perp}{\tau_\parallel} = \frac{\tau_{iv}}{\tau_p}\left(\frac{\lambda_{VZ}}{\lambda_R}\right)^2 + \frac{1}{2}. \qquad \text{Equation 3.7-6}$$

It is theoretically[24] predicted that the ratio of the spin lifetimes for the out-of-plane spins to the in-plane spins for graphene on WSe_2 is ≈20, this is one order more than that observed in graphene on SiO_2 substrate[24]. Experiments have observed a spin relaxation anisotropy ($\tau_\perp/\tau_l$) of ~10 in graphene covered by a single-layer ($MoSe_2$)[25] and multilayers (WS_2)[26] of TMD.

3.7.3 Spin-orbit coupling in bi-layer graphene

Bi-layer graphene (BLG) consists of two layers of graphene existing in AB form (Bernal stacked)[27] than the less likely AA form[28]. BLG, unlike the single-layer graphene, possesses a tunable bandgap controlled by the applied transverse gate electric field[29–31]; however, the bandgap saturates at a value of 0.3 eV. The basic electronic band structure of the bilayer graphene is well understood; yet, when one considers the realistic spin-orbit interaction especially with the electric field gating, the electronic spectrum changes. In 2012, Konschuh et al.[32] calculated the electronic band structure of the AB BLG from first principles in the presence of SOC and considering a transverse electric field. They found that the spin-orbit effects in BLG arise almost solely from the d orbitals. Around the K points, the intrinsic spin-orbit splitting (anticrossing) is about 24 μeV for the low-energy valence and conduction bands. They also considered a transverse electric field which breaks the inversion symmetry leading to an induced Rashba type SOC. The Rashba SOC leads to the opening of bandgap which is linearly proportional to the applied electric field. At the K points, they observed that the spin splitting was about 24 μeV and was independent of the applied electric field. Away from the K points however, with an applied electric field, the Rashba SOC was seen to dominate and leading to a splitting of 10 μeV per field of 1 V/nm; and it showed a linear dependence on the applied electric field.

For BLG encapsulated between hexagonal boron nitride, ab initio calculations indicated the existence of a spin splitting with a similar magnitude as that of isolated BLG sheets[32]. In this case, the intrinsic SOC is in the out-of-plane direction to the BLG plane, while the electric field induced Rashba SOC is in-plane. This leads to an anisotropy in the spin relaxation with intrinsic SOC dephasing only the in-plane spins, whereas, the Rashba SOC de-phases both the in-plane and the out-of-plane spins. It was observed experimentally that the anisotropy in such systems is around 8±2 near the charge neutrality point at 75 K[33] and up to ~12 at 100

K[34].

3.7.4 Spin-orbit coupling in BLG in the proximity of TMD

Electronic band structure of a BLG on WSe_2 (which is a TMD) has been studied from first principles by Gmitra et al.[35], and they found that an indirect bandgap of 12 meV opens up in BLG due to the built-in electric field across the BLG/WSe_2 heterostructure. Here, the valence band is formed by the nondimer carbon atom orbitals of the graphene layer adjacent to TMD, and the conduction band is formed by the nondimer carbon atom orbitals of the graphene layer away from the TMD. Interestingly the spin-orbit coupling of the valence band is huge (of the order 2 meV) and is two orders of magnitude higher in comparison to that of the conduction band. Further, the intrinsic bandgap of BLG on WSe_2 can be tuned or even reversed (the characters of the valence and conduction bands flip) by an application of the external electric field of the order 1 V/nm.

Similar theoretical observations have also been reported by Khoo et al.[36] for BLG/WS_2 system, wherein the SOC is tunable with an application of an electric field across the BLG/WS_2 heterostructure. Further, recent experimental observations[23,37] of weak anti-localisation in BLG/TMD heterostructure is a confirmation of strong SOC induced in BLG.

3.8 Spin absorption at the TMD/graphene interface

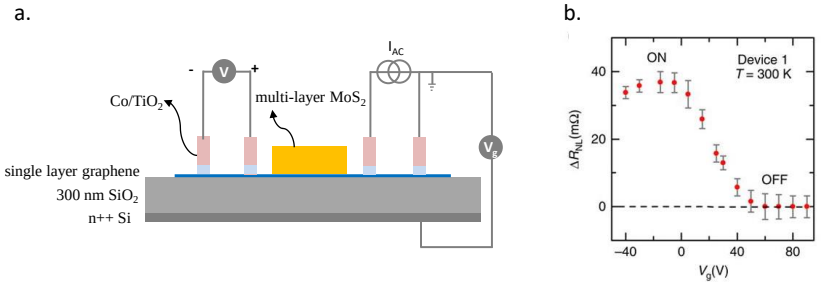

Figure 3.8-1 (a). Device schematic and non-local SV measurement geometry of MoS_2/graphene heterostructure on a 300 nm SiO_2 substrate with n++ Si back gate contacted with the ferromagnetic Co electrode and TiO_2 tunnel barrier. (b). Non-local resistance change (ΔR_{NL}) measured as a function of the applied back gate voltage V_g; the plot is extracted from the report by Dankert et al.[38] in Nature communications.

In the reports of Dankert et al.[38] and Yan et al.[39], spin transport in multi-layer MoS_2/graphene heterostructures was studied; here, the graphene was placed on a silicon substrate, MoS_2 partially covering the graphene and graphene contacted by Co FM contacts with TiO_2 tunnel barrier, as shown in Figure 3.8-1 (a). The change in the non-local resistance (ΔR_{NL}) was measured for the measurement configuration of Figure 3.8-1 as explained in section 3.5.2. ΔR_{NL} was measured as a function of back gate voltage, V_g as shown in Figure 3.8-1 (b). Both the groups independently observed that the ΔR_{NL} changes as a function of V_g and becomes nearly zero at $V_g > 40$ V. $\Delta R_{NL} = 0\ \Omega$ signifies that there is no detectable spin transport across the graphene region covered by MoS_2. Further, they measured the electrical conductivity of

MoS_2 and found that the MoS_2 starts conducting with the application of positive V_g while the ΔR_{NL} approaches 0 Ω. However, MoS_2 was found to behave as an insulator at negative V_g.

Both the groups attribute the change in ΔR_{NL} as a function of V_g to be resulting from the relative change in absorption of spins at the MoS_2/graphene interface. Dankert et al.[38] associated this spin absorption to the change in Schottky barrier at the MoS_2/graphene interface, while Yan et al.[39] regarded the spin absorption to be due to the difference in spin resistance for graphene and MoS_2.

- Dankert et al.[38] directly measured the charge transport (as a function of V_g and temperature) along the MoS_2, MoS_2/graphene interface and graphene by placing an electrode on MoS_2 and another electrode on graphene. They determined that there exists a gate tunable Schottky barrier (Φ) at the MoS_2/graphene interface and they estimated the value of Φ to be changing from 300 meV to 50 meV using the thermionic emission model. For $\Delta R_{NL} = 0$ Ω , they concluded that the Schottky barrier was 50 meV; and with this lowered Φ, the spins could easily enter the MoS_2 where they eventually relax due to the low spin relaxation time in MoS_2.
- Yan et al.[39] calculated the spin resistance for both MoS_2 (R_{MoS_2}) and graphene ($R_{graphene}$) using the definition of Equation 3.4-2. They obtained $R_{graphene} = 408$ Ω and $R_{MoS_2} = 2.7$ Ω at $V_g = 40$ V; and since $R_{MoS_2} < R_{graphene}$, they attribute it to the ability of MoS_2 to absorb spins from the graphene channel resulting in the measured ΔR_{NL} of 0 Ω.

However, both these reports do not consider the effect of TMD induced SOC in graphene as discussed in section 3.7.2, which could change with the applied gate voltage and magnetic field and possibly result in a change in ΔR_{NL}. Hence, it remains a challenge to understand the role and interplay of both the TMD induced SOC in graphene and the spin absorption at the TMD/graphene interface.

References

1. Wilson, J. A. & Yoffe, A. D. The transition metal dichalcogenides discussion and interpretation of the observed optical, electrical and structural properties. Adv. Phys. **18**, 193–335 (1969).

2. Fivaz, R. & Mooser, E. Mobility of Charge Carriers in Semiconducting Layer Structures. Phys. Rev. **163**, 743–755 (1967).

3. Fivaz, R. & Mooser, E. Electron-Phonon Interaction in Semiconducting Layer Structures. Phys. Rev. **136**, A833--A836 (1964).

4. Zhang, C. et al. Bandgap reduction in van der Waals layered 2D materials via a de-charge transfer mechanism. Nanoscale **10**, 16759–16764 (2018).

5. Li, L. et al. Black phosphorus field-effect transistors. Nat. Nanotechnol. **9**, 372 (2014).

6. Sangwan, V. K. & Hersam, M. C. Electronic Transport in Two-Dimensional Materials. Annu. Rev. Phys. Chem. **69**, 299–325 (2018).

7. Novoselov, K. S. et al. Electric field in atomically thin carbon films. Science (80-.). **306**, 666–669 (2004).

8. Radisavljevic, B., Radenovic, A., Brivio, J., Giacometti, V. & Kis, A. Single-layer MoS2 transistors. Nat. Nanotechnol. **6**, 147 (2011).

9. Madhushankar, B. N. et al. Electronic properties of germanane field-effect transistors. 2D Mater. **4**, 21009 (2017).

10. Geim, A. K. & Novoselov, K. S. The rise of graphene. Nat. Mater. **6**, 183–191 (2007).

11. Kane, C. L. & Mele, E. J. Quantum Spin Hall Effect in Graphene. Phys. Rev. Lett. **95**, 226801 (2005).

12. Huertas-Hernando, D., Guinea, F. & Brataas, A. Spin-orbit coupling in curved graphene, fullerenes, nanotubes, and nanotube caps. Phys. Rev. B **74**, 155426 (2006).

13. Fabian, J., Matos-Abiague, A., Ertler, C., Stano, P. & Žutić, I. Semiconductor spintronics. Acta Phys. Slovaca. Rev. Tutorials **57**, 565–907 (2007).

14. Volmer, F. et al. Contact-induced charge contributions to non-local spin transport measurements in Co/MgO/graphene devices. 2D Mater. **2**, 24001 (2015).

15. Raes, B. et al. Determination of the spin-lifetime anisotropy in graphene using oblique spin precession. Nat. Commun. **7**, 11444 (2016).

16. Ringer, S. et al. Measuring anisotropic spin relaxation in graphene. Phys. Rev. B **97**, 205439 (2018).

17. Evgeny Y. Tsymbal, I. Z. Handbook of Spin Transport and Magnetism. Handbook of Spin Transport and Magnetism (2011). doi:10.1201/b11086

18. Manchon, A., Koo, H. C., Nitta, J., Frolov, S. M. & Duine, R. A. New perspectives for Rashba spin–orbit coupling. Nat. Mater. **14**, 871 (2015).

19. Min, H. et al. Intrinsic and Rashba spin-orbit interactions in graphene sheets. Phys. Rev. B **74**, 165310 (2006).

20. Gmitra, M., Konschuh, S., Ertler, C., Ambrosch-Draxl, C. & Fabian, J. Band-structure topologies of graphene: Spin-orbit coupling effects from first principles. Phys. Rev. B **80**, 235431 (2009).

21. Wang, Z. et al. Strong interface-induced spin–orbit interaction in graphene on WS2. Nat. Commun. **6**, 8339 (2015).

22. Avsar, A. et al. Spin–orbit proximity effect in graphene. Nat. Commun. **5**, 4875 (2014).

23. Wang, Z. et al. Origin and magnitude of 'designer' spin-orbit interaction in graphene on semiconducting transition metal dichalcogenides. Phys. Rev. X **6**, 1–15 (2016).

24. Cummings, A. W., Garcia, J. H., Fabian, J. & Roche, S. Giant Spin Lifetime Anisotropy in Graphene Induced by Proximity Effects. Phys. Rev. Lett. **119**, 206601 (2017).

25. Ghiasi, T. S., Ingla-Aynés, J., Kaverzin, A. A. & van Wees, B. J. Large Proximity-Induced Spin Lifetime Anisotropy in Transition-Metal Dichalcogenide/Graphene Heterostructures. Nano Lett. **17**, 7528–7532 (2017).

26. Benítez, L. A. et al. Strongly anisotropic spin relaxation in graphene–transition metal dichalcogenide heterostructures at room temperature. Nat. Phys. **14**, 303–308 (2018).

27. Yan, K., Peng, H., Zhou, Y., Li, H. & Liu, Z. Formation of Bilayer Bernal Graphene: Layer-by-Layer Epitaxy via Chemical Vapor Deposition. Nano Lett. **11**, 1106–1110 (2011).

28. Liu, Z., Suenaga, K., Harris, P. J. F. & Iijima, S. Open and Closed Edges of Graphene Layers. Phys. Rev. Lett. **102**, 15501 (2009).

29. Min, H., Sahu, B., Banerjee, S. K. & MacDonald, A. H. Ab initio theory of gate induced gaps in graphene bilayers. Phys. Rev. B **75**, 155115 (2007).

30. Castro, E. V et al. Biased Bilayer Graphene: Semiconductor with a Gap Tunable by the Electric Field Effect. Phys. Rev. Lett. **99**, 216802 (2007).

31. Zhang, Y. et al. Direct observation of a widely tunable bandgap in bilayer graphene. Nature **459**, 820 (2009).

32. Konschuh, S., Gmitra, M., Kochan, D. & Fabian, J. Theory of spin-orbit coupling in bilayer graphene. Phys. Rev. B **85**, 115423 (2012).

33. Leutenantsmeyer, J. C., Ingla-Aynés, J., Fabian, J. & van Wees, B. J. Observation of Spin-Valley-Coupling-Induced Large Spin-Lifetime Anisotropy in Bilayer Graphene. Phys. Rev. Lett. **121**, 127702 (2018).

34. Xu, J., Zhu, T., Luo, Y. K., Lu, Y.-M. & Kawakami, R. K. Strong and Tunable Spin-Lifetime Anisotropy in Dual-Gated Bilayer Graphene. Phys. Rev. Lett. **121**, 127703 (2018).

35. Gmitra, M. & Fabian, J. Proximity Effects in Bilayer Graphene on Monolayer WSe2: Field-Effect Spin Valley Locking, Spin-Orbit Valve, and Spin Transistor. Phys. Rev. Lett. **119**, 146401 (2017).

36. Khoo, J. Y., Morpurgo, A. F. & Levitov, L. On-Demand Spin–Orbit Interaction from Which-Layer Tunability in Bilayer Graphene. Nano Lett. **17**, 7003–7008 (2017).

37. Afzal, A. M. et al. Gate Modulation of the Spin-orbit Interaction in Bilayer Graphene Encapsulated by WS2 films. Sci. Rep. **8**, 3412 (2018).

38. Dankert, A. & Dash, S. P. Electrical gate control of spin current in van der Waals heterostructures at room temperature. Nat. Commun. **8**, 16093 (2017).

39. Yan, W. et al. A two-dimensional spin field-effect switch. Nat. Commun. **7**, 13372 (2016).